Applied Thermal Engineering 155 (2019) 637–649

Contents lists available at ScienceDirect

Applied Thermal Engineering

journal homepage: www.elsevier.com/locate/apthermeng

Research Paper

Numerical investigation on bubble dynamics during pool nucleate boiling in presence of a non-uniform electric field by LBM

Yuan Feng[a], Huixiong Li[a,*], Kaikai Guo[a], Xianliang Lei[a], Jianfu Zhao[b,c]

[a] State Key Laboratory of Multiphase Flow in Power Engineering, Xi'an Jiaotong University, Xi'an 710049, China
[b] CAS Key Laboratory of Microgravity, Institute of Mechanics, Chinese Academy of Sciences, Beijing 100190, China
[c] School of Engineering Science, University of Chinese Academy of Sciences, Beijing 100049, China

HIGHLIGHTS

- A numerical model was built to simulate the pool boiling under an electric field.
- The single bubble nucleate boiling under a radial electric field was simulated.
- A radial electric field could accelerate the departure of the vapor bubble.
- Decreasing gravity could enhance the effect of electric field on bubble dynamics.
- The total electric field force increased firstly and then decreased over time.

ARTICLE INFO

Keywords:
Lattice Boltzmann method
Electrohydrodynamics
Bubble departure diameter
Bubble release frequency

ABSTRACT

Previous experimental studies proved that an external electric field could accelerate the detachment of vapor bubble. However, it was difficult to investigate the influencing mechanism of an electric field on bubble dynamics because of the limit of experimental technical methods. To solve this problem, a two-dimensional lattice Boltzmann model was developed in this paper to simulate the pool boiling in presence of an external electric field by coupling the pseudopotential model with phase-change model and electric field model. The growth and detachment of a single bubble on a horizontal wall during pool nucleate boiling with a non-uniform electric field was simulated. The influence of gravitational acceleration and electric field intensity on bubble dynamics was investigated in detail, and the influencing mechanism of an external electric field on bubble dynamics during pool nucleate boiling was analyzed. The numerical results showed that increasing electric filed intensity could decrease both bubble departure diameter and bubble release period. Decreasing gravitational acceleration could strengthen the influence of electric field intensity on bubble departure diameter and bubble release frequency. In other words, the non-uniform electric field established at present study could effectively reduce the possibility of heat transfer deterioration under microgravity.

1. Introduction

Pool nucleate boiling is a highly efficient way of heat transfer with the characteristics of low wall superheat and high heat flux. It has been widely applied in various fields of the engineering technology, such as nuclear reactors, steam generators, and micro-electronic devices. In aerospace field, the increasing demand of large spacecraft for thermal management system transcended the capacity of traditional single-phase liquid thermal control technology. Boiling heat transfer is a good option to solve this problem. However, the detachment of vapor bubble becomes much harder due to the condition of microgravity. This situation might lead to the reduction of heat transfer capacity and even the burnout of the heated surface.

Electrohydrodynamic (EHD) is an effective way to enhance the boiling heat transfer under microgravity. Using experimental method, some researchers studied the effect of EHD on bubble dynamics and heat transfer during pool boiling [1–6]. These authors performed numerous experimental researches, obtained abundant experimental data and proved that an external electric field could obviously affect heat transfer and bubble dynamics during pool boiling. However, it is difficult to obtain some microscopic details (such as the distribution of electric field intensities and electric field forces at the phase interface)

* Corresponding author.
E-mail address: huixiong@mail.xjtu.edu.cn (H. Li).

https://doi.org/10.1016/j.applthermaleng.2019.04.110
Received 1 November 2018; Received in revised form 13 April 2019; Accepted 25 April 2019

Nomenclature

a,b,R,ω	parameters in Peng-Robinson EOS
Bo_e	electric Bond number
c_v	specific heat at constant volume
D_d	bubble departure diameter
$\mathbf{e}_\alpha$	lattice velocity vector
$\mathbf{E}$	electric field intensity
f_α, $\mathbf{f}$	distribution function for density
$\mathbf{F}$	external force
F_α'	forcing term in the velocity space
$\mathbf{F}_{\text{ads}}$	fluid-solid interaction force
$\mathbf{F}_{\text{e}}$	electric force
$\mathbf{F}_{\text{g}}$	gravity
$\mathbf{F}_{\text{m}}$	intermolecular interaction force
$\mathbf{g}$	gravitational acceleration
G	Interaction strength
G_w	a parameter to tune the contact angle
h_{fg}	latent heat of vaporization
Ja	Jacob number
L_x, L_y	width and height of computational domain
$\mathbf{M}$	orthogonal transformation matrix
p	pressure
p_{EOS}	prescribed non-ideal equation of state
R	radius of bubble / droplet
$s(\mathbf{x})$	switch function
$\mathbf{S}$	forcing term in the moment space
t	time
T	temperature
T_{sat}	saturation temperature
T_w	temperature of the heating surface
$\mathbf{u}$	fluid velocity
V	electric potential
w_α	weighting coefficient
$\mathbf{x}$	position

Greek symbols

Δt	time step
ΔT	wall superheat
$\mathbf{\Lambda}$	diagonal matrix of relaxation time
τ	relaxation time
ν	kinematic coefficient of viscosity
ρ	density
σ	parameter to tune the mechanical stability
ψ	pseudopotential
λ	thermal conductivity
ε_0	the permittivity of vacuum
ε	the relative permittivity of fluid
η_α	distribution function for electric potential
χ	thermal diffusion coefficient
γ	surface tension

Subscripts and superscripts

0	characteristic properties
α	lattice direction
c	critical properties
L, V	liquid, vapor
s	solid
x, y	direction
eq	equilibrium properties

by experimental method. Therefore, experimental method is incapable of studying the influencing mechanism of an electric field on bubble dynamics during pool nucleate boiling. Numerical method is a good choice to solve this problem.

Until now, some scholars numerically investigated different EHD phenomena, such as the deformation of a droplet in a uniform electric field and a rising bubble under an external electric field [7–9]. These numerical investigations laid a foundation for studying the influence of EHD on bubble dynamics during nucleate boiling or film boiling, which has been studied by many scholars using various numerical methods [10–13]. Welch and Biswas [10] employed level-set method to simulate the film boiling under a uniform electric field, and they found that wall temperature decreased with an increase in electric field intensity at a given heat flux condition. Tomar et al. [11] and Pandey et al. [12] simulated the effect of a uniform electric field on film boiling under different gravitational accelerations by CLSVOF method, and these authors found that increasing electric field intensity could increase both the averaged Nusselt number and the bubble release frequency. In addition, the influence of the electric field on film boiling heat transfer would be greater with a decrease in gravitational acceleration. Hristov et al. [13] simulated the growth and detachment of a single bubble during pool nucleate boiling under the effect of a uniform electric field by level-set method, and these authors found that bubble became slender in shape under the effect of a uniform electric field.

However, there were still some problems in previous numerical studies to be solved. Firstly, all of these studies adopted traditional CFD methods, such as level-set method and CLSVOF method. It's well-known that traditional CFD methods are incapable of simulating the process of bubble nucleation, thus a small bubble or vapor film must be located on the heated wall initially when these methods are used to simulate the pool boiling. Secondly, most of previous numerical studies were aimed at the influence of EHD on film boiling, but the simulations of EHD's effect on pool nucleate boiling were extremely rare. Finally, the electric fields adopted in most of previous studies were uniform. However, according to the numerical results of Hristov et al. [13], a uniform electric field had limited effect on bubble dynamics during nucleate boiling. Therefore, a uniform electric field is incapable of accelerating bubble detachment under microgravity condition, and it is necessary to study the effect of a non-uniform electric field on bubble dynamics and heat transfer during pool boiling.

Lattice Boltzmann method (LBM) [14–18] is a mesoscopic method with the advantages of simplicity and convenience. Unlike the traditional CFD, it doesn't solve the differential equations. On the contrary, it only involves a series of collision and stream steps. Besides, it's easy to deal with complex boundaries by LBM. In recent decades, LBM has already been adopted to investigate the multiphase flow phenomena containing liquid-vapor phase change. Based on the phase-field LB method, many numerical simulations [19–24] were performed to study the bubble dynamics and heat transfer during pool boiling. For example, using three-dimensional (3D) LB model, the saturated nucleate boiling and film boiling were simulated and the influence of wall superheat and gravitational acceleration on bubble dynamics and heat transfer during nucleate boiling and film boiling were studied by Sadeghi et al. [21,22].

Due to its kinetic nature and automatic phase separation via an inter-particle potential, the pseudopotential LB model [25] received extensive attention and has been utilized to simulate liquid-vapor phase change phenomenon. Hazi and Markus [26] simulated the growth of vapor bubble on a heated wall, and these authors also studied the influence of gravitational acceleration on bubble departure diameter and bubble release frequency. Gong and Cheng [27,28] proposed an improved phase-change model and simulated the pool boiling processes under different wall superheats, and these authors also investigated the effect of wettability on boiling curves and critical heat flux (CHF). Using

the same model, Ma et al. [29] studied the influence of gravitational acceleration and heater's size on boiling curves. Li et al. [30] proposed a hybrid thermal LB model to simulate pool boiling processes under different wall superheats, and these authors also investigated the effect of wettability on boiling curves and CHF. However, at present, few scholars applied this model to study bubble dynamics or heat transfer during pool boiling in presence of an external electric field.

In this paper, a two-dimensional LB model was developed to simulate pool boiling processes under the effect of an electric field. In this model, the hybrid thermal LB model proposed by Li et al. [30] was coupled with the electric field model. Bubble dynamics during pool nucleate boiling under different gravitational accelerations and electric field intensities were simulated. The influence of gravitational acceleration and electric field intensity on bubble departure diameter and bubble release frequency was analyzed, and the effect of a non-uniform electric field on bubble dynamics was also investigated in detail. The numerical study in this paper provided an important basis for further analysis of the influencing mechanism of EHD on bubble dynamics and heat transfer during pool nucleate boiling.

2. Numerical methods

2.1. Two-phase flow model

The Multiple-Relaxation-Time (MRT) pseudopotential multiphase LB model is used to solve the distribution of phase fields and flow fields. The LB equations [30], which govern the evolution of the density distribution function, can be written as Eqs. (1) and (2).

$$f_\alpha^*(\mathbf{x}, t) = f_\alpha(\mathbf{x}, t) - (\mathbf{M}^{-1}\mathbf{\Lambda}\mathbf{M})_{\alpha\beta}(f_\beta - f_\beta^{eq}) + \Delta t F_\alpha' \tag{1}$$

$$f_\alpha(\mathbf{x} + \mathbf{e}_\alpha\Delta t, t + \Delta t) = f_\alpha^*(\mathbf{x}, t) \tag{2}$$

where, Eqs. (1) and (2) are the steps of collision and stream, respectively. f_α is the distribution function of density, and $f_\alpha{}^{eq}$ is its equilibrium distribution function. F_α' is the forcing term in the velocity space. $\mathbf{M}$ is an orthogonal transformation matrix [14]. $\mathbf{e}_\alpha$ is the discrete velocity along the α^{th} direction. For the D2Q9 model, $\mathbf{M}$ and $\mathbf{e}_\alpha$ can be expressed as Eq. (3) and Eq. (4), respectively. $\mathbf{\Lambda}$ is a diagonal matrix which consists of relaxation times, and it can be expressed as Eq. (5).

$$\mathbf{M} = \begin{bmatrix} 1 & 1 & 1 & 1 & 1 & 1 & 1 & 1 & 1 \\ -4 & -1 & -1 & -1 & -1 & 2 & 2 & 2 & 2 \\ 4 & -2 & -2 & -2 & -2 & 1 & 1 & 1 & 1 \\ 0 & 1 & 0 & -1 & 0 & 1 & -1 & -1 & 1 \\ 0 & -2 & 0 & 2 & 0 & 1 & -1 & -1 & 1 \\ 0 & 0 & 1 & 0 & -1 & 1 & 1 & -1 & -1 \\ 0 & 0 & -2 & 0 & 2 & 1 & 1 & -1 & -1 \\ 0 & 1 & -1 & 1 & -1 & 0 & 0 & 0 & 0 \\ 0 & 0 & 0 & 0 & 0 & 1 & -1 & 1 & -1 \end{bmatrix} \tag{3}$$

$$\mathbf{e}_\alpha = \begin{bmatrix} 0 & 1 & 0 & -1 & 0 & 1 & -1 & -1 & 1 \\ 0 & 0 & 1 & 0 & -1 & 1 & 1 & -1 & -1 \end{bmatrix} \tag{4}$$

$$\mathbf{\Lambda} = \text{diag}(\tau_\rho^{-1}, \tau_e^{-1}, \tau_\varsigma^{-1}, \tau_j^{-1}, \tau_q^{-1}, \tau_j^{-1}, \tau_q^{-1}, \tau_\nu^{-1}, \tau_\nu^{-1}) \tag{5}$$

The dot product between Eq. (1) and $\mathbf{M}$ can be expressed as Eq. (6).

$$\mathbf{m}^* = \mathbf{m} - \mathbf{\Lambda}(\mathbf{m} - \mathbf{m}^{eq}) + \Delta t(\mathbf{I} - \frac{\mathbf{\Lambda}}{2})\mathbf{S} \tag{6}$$

where, $\mathbf{m} = \mathbf{M}\mathbf{f}$, $\mathbf{m}^{eq} = \mathbf{M}\mathbf{f}^{eq}$ and $\mathbf{m}^* = \mathbf{M}\mathbf{f}^*$. $\mathbf{m}^{\text{eq}}$ can be calculated by Eq. (7), $\mathbf{I}$ is the unit tensor, and $\mathbf{S}$ is the forcing term in the moment space [30] and can be expressed as Eq. (8).

$$\mathbf{m}^{eq} = \rho(1, -2 + 3|\mathbf{u}|^2, 1 - 3|\mathbf{u}|^2, u_x, -u_x, u_y, -u_y, u_x^2 - u_y^2, u_x u_y)^T \tag{7}$$

$$\mathbf{S} = \Big[0, 6\mathbf{u}\cdot\mathbf{F} + \frac{\sigma|\mathbf{F}_m|^2}{\psi^2\Delta t(\tau_e - 0.5)}, -6\mathbf{u}\cdot\mathbf{F} - \frac{\sigma|\mathbf{F}_m|^2}{\psi^2\Delta t(\tau_\varsigma - 0.5)}, F_x, -F_x, F_y, -F_y, 2(u_xF_x - u_yF_y), u_xF_y + u_yF_x^T\Big] \tag{8}$$

In Eq. (7), $\mathbf{u}$ is the macroscopic velocity. Macroscopic density ρ and velocity $\mathbf{u}$ can be calculated by Eq. (9). $\mathbf{F}$ is the total force, including intermolecular interaction force $\mathbf{F}_{\text{m}}$, fluid-solid interaction force $\mathbf{F}_{\text{ads}}$, buoyant force $\mathbf{F}_{\text{g}}$ and electric field force $\mathbf{F}_{\text{e}}$. $\mathbf{F}_{\text{m}}$, $\mathbf{F}_{\text{ads}}$ and $\mathbf{F}_{\text{g}}$ can be calculated respectively by Eqs. (10)–(12). In Eq. (18), σ is an parameter for tuning the mechanical stability condition. The specific description about σ can be referred to Ref. [31].

$$\rho = \sum_\alpha f_\alpha,\ \rho\mathbf{u} = \sum_\alpha \mathbf{e}_\alpha f_\alpha + 0.5\Delta t\mathbf{F} \tag{9}$$

$$\mathbf{F}_m = -3G\psi(\mathbf{x})\sum_{\alpha=1}^{8} w_\alpha\psi(\mathbf{x} + \mathbf{e}_\alpha)\mathbf{e}_\alpha \tag{10}$$

$$\mathbf{F}_{\text{ads}} = -G_w\psi(\mathbf{x})\sum_{\alpha=1}^{8} w_\alpha\psi(\mathbf{x})s(\mathbf{x} + \mathbf{e}_\alpha)\mathbf{e}_\alpha \tag{11}$$

$$\mathbf{F}_{\text{g}} = (\rho - \rho_{ave})\mathbf{g} \tag{12}$$

In Eq. (10), w_α are the weights. $w_0 = 4/9$, $w_{1\text{-}4} = 1/9$ and $w_{5\text{-}8} = 1/36$. G is the intermolecular interaction strength. ψ is the pseudopotential, and can be calculated by Eq. (13). In Eq. (11), G_w is fluid-solid interaction strength which could tune the contact angle. $s(\mathbf{x} + \mathbf{e}_\alpha)$ is a switch function that equals 1 for solid phase and 0 for fluid phase. In Eq. (12), ρ_{ave} is the average density in the whole computational domain. $\mathbf{g} = (0, -g)$ is the gravitational acceleration.

$$\psi(\mathbf{x}) = \sqrt{\frac{6p_{EOS} - 2\rho}{3G}} \tag{13}$$

where p_{EOS} is the prescribed non-ideal equation of state.

In this study, Peng-Robinson (P-R) equation of state is adopted to calculate p_{EOS}.

$$p_{EOS} = \frac{\rho RT}{1 - b\rho} - \frac{a[1 + (0.37464 + 1.54226\omega - 0.26992\omega^2)(1 - \sqrt{T/T_c})]^2\rho^2}{1 + 2b\rho - b^2\rho^2} \tag{14}$$

where $a = 0.45724R^2{T_c}^2/p_c$, $b = 0.0778RT_c/p_c$, T_c and p_c are critical temperature and critical pressure, respectively. In this study, the parameters in Eqs. (8) and (14) take the same value as those in Ref. [30]: $\sigma = 1.2$, $\omega = 0.344$, $a = 3/49$, $b = 2/21$, $R = 1$, $T_c = 0.109383$ and $p_c = 0.089355$.

2.2. Liquid-vapor phase-change model

According to the local balance law for entropy, the energy equation with phase-change source term [30] (neglecting the viscous heat dissipation) can be expressed as Eq. (15).

$$\frac{\partial T}{\partial t} + \mathbf{u}\cdot\nabla T = \frac{1}{\rho c_v}\nabla\cdot(\lambda\nabla T) - \frac{T}{\rho c_v}\Big(\frac{\partial p_{\text{EOS}}}{\partial T}\Big)_\rho\nabla\cdot\mathbf{u} \tag{15}$$

On the right-hand side of Eq. (15), the first term is the thermal diffusive term and the second term is the phase-change source term. λ is the thermal conductivity, and c_v is the specific heat. Eq. can be rewritten as Eq. (15), and the right-hand side of Eq. (16) is defined as $K(T)$. Eq. (16) is solved by finite-difference method and the fourth-order Runge-Kutta scheme is adopted for time discretization.

$$\frac{\partial T}{\partial t} = -\mathbf{u}\cdot\nabla T + \frac{1}{\rho c_v}\nabla\cdot(\lambda\nabla T) - \frac{T}{\rho c_v}\Big(\frac{\partial p_{\text{EOS}}}{\partial T}\Big)_\rho\nabla\cdot\mathbf{u} \equiv K(T) \tag{16}$$

$$T(t + \Delta t) = T(t) + \frac{\Delta t}{6}(h_1 + 2h_2 + 2h_3 + h_4) \tag{17}$$

where, $h_1 \sim h_4$ can be calculated by

$$h_1 = K(T(t)), \quad h_2 = K(T(t) + \frac{\Delta t}{2}h_1), \quad h_3 = K(T(t) + \frac{\Delta t}{2}h_2), \quad h_4 = K(T(t) + \Delta t h_3) \tag{18}$$

2.3. Electric field model for perfect dielectric

Based on the electrohydrodynamics theory, the electric force $\mathbf{F_e}$ can be expressed as Eq. (19).

$$\mathbf{F_e} = q_v\mathbf{E} - \frac{1}{2}\mathbf{E}\cdot\mathbf{E}\nabla\varepsilon\varepsilon_0 + \frac{\varepsilon_0}{2}\nabla(\rho\frac{\partial\varepsilon}{\partial\rho}\mathbf{E}\cdot\mathbf{E}) \tag{19}$$

where, q_v is the free charge density, $\mathbf{E}$ is the electric field intensity, ε_0 is the vacuum permittivity and ε is the relative permittivity of fluid. On the right-hand side of Eq. (19), the first term, second term and third term represent Coulomb force, dielectric electrophoretic force and electrostriction force, respectively.

In this study, the following assumptions are made: (1) The fluid is incompressible and perfect dielectric; (2) There is no dynamic current in the fluid and the magneto-induced effect is neglected; (3) The electric field vectors are irrotational. Based on these assumptions, the Coulomb force and the electrostriction force can be neglected, the electric force $\mathbf{F_e}$ can be simplified [32] into Eq. (20) and the electric field intensity $\mathbf{E}$ could be solved by Eq. (21).

$$\mathbf{F_e} = -\frac{1}{2}\mathbf{E}\cdot\mathbf{E}\nabla\varepsilon\varepsilon_0 \tag{20}$$

$$\nabla\cdot(\varepsilon\varepsilon_0\mathbf{E}) = 0 \tag{21}$$

Since electric field intensity $\mathbf{E}$ could be expressed as the gradient of electric potential V, i.e., $\mathbf{E} = -\nabla V$, Eq. (21) can be rewritten as Eq. (22). In this study, Eq. (22) can be solved by the LB equation [33], as shown in Eq. (23).

$$\nabla\cdot(\varepsilon\varepsilon_0\nabla V) = 0 \tag{22}$$

$$\eta_\alpha(\mathbf{x} + \mathbf{e}_\alpha\Delta t, t + \Delta t) - \eta_\alpha(\mathbf{x}, t) = -\frac{1}{\tau_s}[\eta_\alpha(\mathbf{x}, t) - \eta_\alpha^{eq}(\mathbf{x}, t)] \tag{23}$$

where τ_s is the relaxation time, $\tau_s = 3\varepsilon\varepsilon_0 + 0.5$. η_α is the distribution function of electric potential, and $\eta_\alpha{}^{eq}(\mathbf{x},t)$ is its equilibrium distribution function that can be calculated by Eq. (24). And electric potential V can be calculated by Eq. (25).

$$\eta_\alpha^{eq}(\mathbf{x}, t) = w_\alpha V \tag{24}$$

$$V = \sum_\alpha \eta_\alpha(\mathbf{x}, t) \tag{25}$$

3. Validation of numerical models

3.1. Validation of phase-change model

In order to validate the rationality of phase-change model, the droplet evaporation processes are simulated in an environment with negligible viscous heat dissipation and no buoyancy. According to the previous studies, the time rate of change of the square of the evaporating droplet diameter is constant, i.e., $D^2(t)/D_0{}^2 = 1\text{-}kt$ [34]. The simulations are carried out in a square computational domain with a grid size of $L_x \times L_y$. Initially, a droplet with a diameter of D_0 is located in the center of the computational domain. The temperature of the droplet is set to be its saturated temperature $T_{sat} = 0.86T_c$, while a temperature of T_g is applied to the surrounding vapor of the droplet. The densities of liquid and vapor are $\rho_L = 6.5$ and $\rho_V = 0.38$, respectively.

Eqs. (26)–(29) are used to calculate the distribution function of density (i.e., f_α) at top boundary ($y = L_y$), bottom boundary ($y = 0$), left boundary ($x = 0$) and right boundary ($x = L_x$), respectively.

Top boundary ($y = L_y$):

$$f_4 = f_2, \quad f_7 = f_5 + \frac{1}{2}(f_1 - f_3) + \frac{1}{4}(F_x + F_y), \quad f_8 = f_6 - \frac{1}{2}(f_1 - f_3) - \frac{1}{4}(F_x - F_y) \tag{26}$$

Bottom boundary ($y = 0$):

$$f_2 = f_4, \quad f_5 = f_7 - \frac{1}{2}(f_1 - f_3) - \frac{1}{4}(F_x + F_y), \quad f_6 = f_8 + \frac{1}{2}(f_1 - f_3) + \frac{1}{4}(F_x - F_y) \tag{27}$$

Left boundary ($x = 0$):

$$f_1 = f_3, \quad f_5 = f_7 - \frac{1}{2}(f_2 - f_4) - \frac{1}{4}(F_x + F_y), \quad f_8 = f_6 + \frac{1}{2}(f_2 - f_4) + \frac{1}{4}(-F_x + F_y) \tag{28}$$

Right boundary ($x = L_x$):

$$f_3 = f_1, \quad f_7 = f_5 + \frac{1}{2}(f_2 - f_4) + \frac{1}{4}(F_x + F_y), \quad f_6 = f_8 - \frac{1}{2}(f_2 - f_4) - \frac{1}{4}(-F_x + F_y) \tag{29}$$

Three cases are simulated, and the calculation parameters used in these simulations are shown in Table 1. The Jacob numbers for Case B and Case C are $Ja = 0.1$ and $Ja = 0.2$, respectively, where $Ja = c_v(T_g - T_{sat})/h_{fg}$ and h_{fg} is the latent heat of vaporization. Fig. 1 represents the evolution of droplet equivalent diameter D simulated by LBM in this paper, with the comparison with the two-dimensional (2D) numerical results of Li et al. [35] and the three-dimensional (3D) numerical results of Sadeghi et al. [21]. As shown in Fig. 1, in all of these three cases, the value of $(D/D_0)^2$ decreases linearly over time. Quantitatively, the parameter k in the law of $D^2(t)/D_0{}^2 = 1\text{-}kt$ is given by 4×10^{-6}, 6×10^{-6} and 1×10^{-5} for Cases A, B and C, respectively. Obviously, the parameter k for Case C is about twice as much as that for Case B. In addition, as shown in Fig. 1, our 2D numerical results agree well with both the 2D numerical results of Li et al. [35] and the 3D numerical results Sadeghi et al. [21]. Therefore, the rationality of the 2D liquid-vapor phase-change model used at present study could be proved.

3.2. Validation of electric field model

In order to validate the rationality of electric field model, the distribution of electric field intensity around a static bubble is simulated. A circular bubble with the diameter of $D_0 = 40$ is located at the center of the computational domain and the size of the computational domain is $5D_0 \times 5D_0$. A uniform electric field is imposed at the vertical direction and the ratio of permittivity between vapor and liquid is set as 0.2 in this section. Besides, the electric potential is $V_0 = 17.5$ at the bottom boundary and 0 at the top boundary, while other boundaries are Neumann boundary conditions. Concretely, Eqs. (30)–(33) are adopted to solve the distribution of electric potential V (i.e., η_α) at top boundary ($y = L_y$), bottom boundary ($y = 0$), left boundary ($x = 0$) and right boundary ($x = L_x$), respectively. The theoretical solution of electric field intensity can be expressed as Eq. (34), where $E_0 = V_0/(5D_0)$ in this section.

Table 1
The calculation parameters used in the simulations of the droplet evaporation processes.

Cases	L_x	L_y	D_0	T_{sat}	T_g	ΔT	c_v	λ
A	200	200	60	$0.86T_c$	T_c	$0.14T_c$	5	2/3
B	100	100	40	$0.86T_c$	T_c	$0.14T_c$	3.29	0.3
C	100	100	40	$0.86T_c$	$1.14T_c$	$0.28T_c$	3.29	0.3

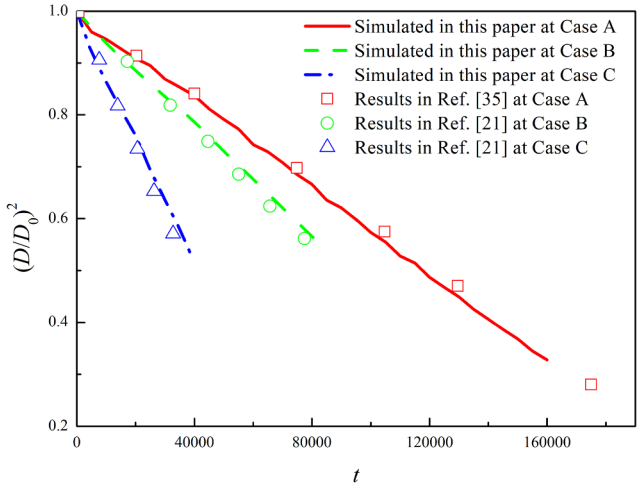

Fig. 1. Variation of D^2 with time simulated by LBM in this paper, with the comparison with the numerical results in Ref. [35] and in Ref. [21].

$$V(x, L_y) = 0, \quad \eta_\alpha(x, L_y) = \eta_\alpha^{eq}(x, L_y) + \eta_\alpha(x, L_y - 1) - \eta_\alpha^{eq}(x, L_y - 1) \tag{30}$$

$$V(x, 0) = V_0, \quad \eta_\alpha(x, 0) = \eta_\alpha^{eq}(x, 0) + \eta_\alpha(x, 1) - \eta_\alpha^{eq}(x, 1) \tag{31}$$

$$V(0, y) = V(1, y), \quad \eta_\alpha(0, y) = \eta_\alpha^{eq}(0, y) + \eta_\alpha(1, y) - \eta_\alpha^{eq}(1, y) \tag{32}$$

$$V(L_x, y) = V(L_x - 1, y), \quad \eta_\alpha(L_x, y) = \eta_\alpha^{eq}(L_x, y) + \eta_\alpha(L_x - 1, y) - \eta_\alpha^{eq}(L_x - 1, y) \tag{33}$$

$$\mathbf{E} = \begin{cases} \frac{2\varepsilon_L E_0}{\varepsilon_V + \varepsilon_L}(\mathbf{i}_r \cos\theta + \mathbf{i}_\theta \sin\theta) & r \leqslant 0.5D_0 \\ [E_0 + \frac{(\varepsilon_V - \varepsilon_L)D_0^2 E_0}{4(\varepsilon_V + \varepsilon_L)r^2}] \sin\theta \mathbf{i}_r - [-E_0 + \frac{(\varepsilon_V - \varepsilon_L)D_0^2 E_0}{4(\varepsilon_V + \varepsilon_L)r^2}] \cos\theta \mathbf{i}_\theta & r > 0.5D_0 \end{cases} \tag{34}$$

Fig. 2(a) displays the distribution of electric field intensities and electric field streamlines simulated by LBM in this paper. As shown in Fig. 2(a), the distributions of electric field intensities and electric streamlines are homogeneous at the interior of bubble and the region far away from the phase interface. However, around the phase interface, the distribution of electric field intensities is not homogeneous and the electric streamlines are distorted. Fig. 2(b) and (c) display the distribution of electric field intensities at $y = 2.5D_0$ and $x = 2.5D_0$, respectively, with the comparison with the analytical solutions. As shown in Fig. 2(b) and (c), our numerical results are in good agreement with the analytical solutions and the maximal error of electric field intensity is 3.6%. Therefore, the electric field model in this paper is capable of simulating the distribution of electric fields in multiphase flows.

4. Numerical results

4.1. Physical model and calculation parameters

In this paper, bubble dynamics during pool nucleate boiling in presence of a non-uniform electric field are simulated in the computational domain with $L_x \times L_y$, as shown in Fig. 3(a). The periodic boundary condition is employed at left and right boundaries, the convective boundary condition is applied at the top boundary and the no-slip boundary condition is applied at the bottom boundary. Initially, the computational domain is filled with saturated liquid, $T_{sat} = 0.86T_c$. The temperature of the bottom wall is fixed at T_{sat} except that a high temperature $T_w = 1.25T_c$ is applied to the three central grids of the wall. At the same time, a radial non-uniform electric field is provided by a charged metal sphere, as shown in Fig. 3(b). The radius of the charged metal sphere is $R_d = 60$ and the distance from the center of the charged metal sphere to the center point of the bottom boundary (i.e., point "A") is $r_h = 80$. The electric potential on the charged metal sphere is V_0, and the electric potential is set to be 0 at infinity. The distribution of electric potential outside the charged metal ball can be expressed as Eq. (35).

$$V = R_d V_0 / r \tag{35}$$

where r is the distance to the center of the charged metal sphere.

The relaxation times in Eq. (5) take the same value as those in Ref. [35]: $\tau_\rho = 1.0$, $\tau_e = 1.25$, $\tau_\varsigma = 1.25$, $\tau_j = 1.0$, $\tau_q = 1/1.1$, and $\tau_\nu = 0.8$. In Eq. (11), the coefficient G_w is equal to 0, thus the contact angle is 44.5°. The value of parameters used at study, such as kinematic viscosity ν, specific heat c_v and thermal diffusion coefficient χ, are given in Table 2. The thermal conductivity of fluid can be calculated by $\lambda = \rho c_v \chi$.

The characteristic length l_0, characteristic velocity u_0 and characteristic time t_0 are defined respectively as Eq. (36).

$$l_0 = \sqrt{\frac{\gamma}{g_0(\rho_L - \rho_V)}}, \quad u_0 = \sqrt{g_0 l_0}, \quad t_0 = \frac{l_0}{u_0} \tag{36}$$

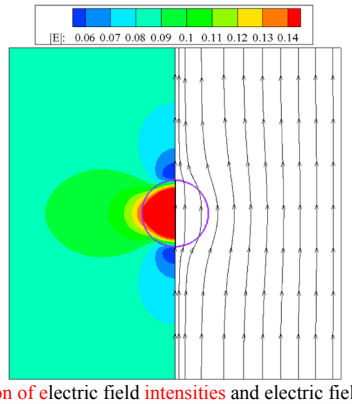

(a) Distribution of electric field intensities and electric field streamlines

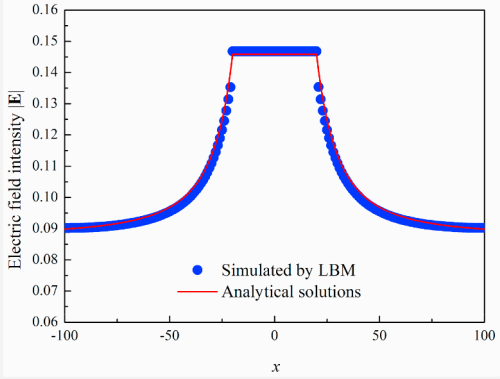

(b) Distribution of electric field intensities at $y = 2.5D_0$

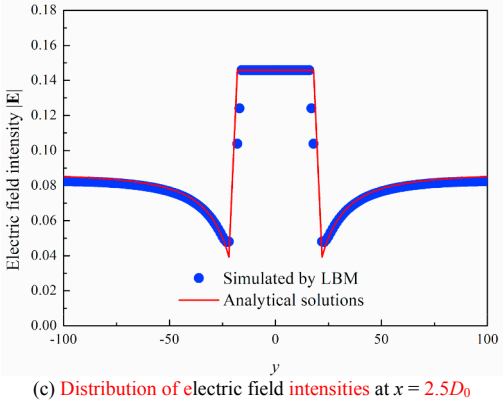

(c) Distribution of electric field intensities at $x = 2.5D_0$

Fig. 2. Distributions of the electric field intensities and the electric streamlines simulated at present study by LBM.

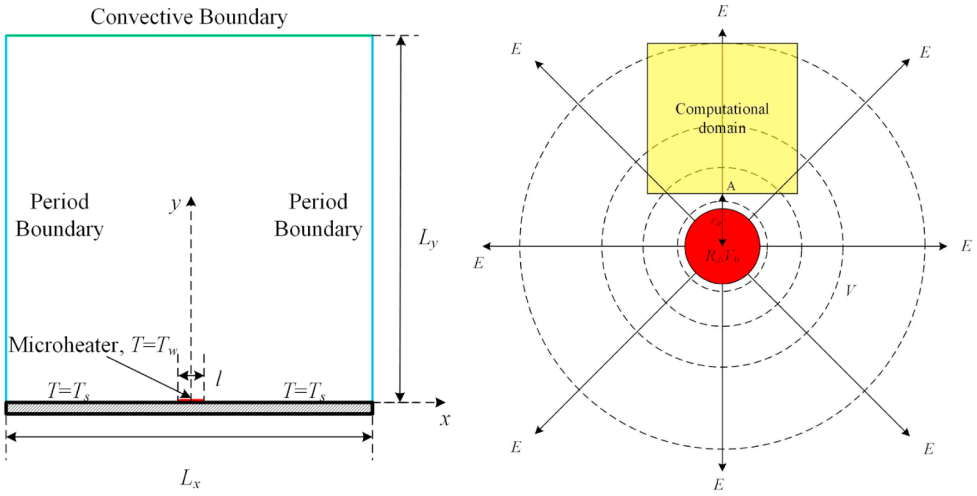

(a) The computational domain for pool nucleate boiling

(b) The establishment of a radial electric field

Fig. 3. The physical model used in the simulations.

Table 2
The unit conversion from lattice unit to physical unit.

Symbols	Lattice unit	Physical unit	Conversion factor
g_0	0.00003	9.8 m/s^2	3.267 × 10^5 m/s^2
γ	0.0878	0.1 N/m	1.139 N/m
ρ_L	6.5	65 kg/m^3	10 kg/m^3
ρ_V	0.38	3.8 kg/m^3	10 kg/m^3
l_0	21.868	0.0129 m	0.00059 m
u_0	0.0256	0.3557 m/s	13.89 m/s
t_0	853.78	0.0363 s	0.0000425 s
ν	0.1	0.00082 m^2/s	0.0082 m^2/s
ΔT	0.04266	20 K	468.82 K
c_v	5	211.94 J/kg·K	42.39 J/kg·K
h_{fg}	0.5032	10000 J/kg	19872.81 J/kg
χ	0.06	0.000492 m^2/s	0.0082 m^2/s
λ_L	1.95	6.78 W/m·K	3.477 W/m·K
λ_V	0.114	0.396 W/m·K	3.477 W/m·K
$\varepsilon_0\varepsilon_L$	2.236	1.98 × 10^{-11}F/m	8.85 × 10^{-12}F/m
$\varepsilon_0\varepsilon_V$	1	8.85 × 10^{-12}F/m	8.85 × 10^{-12}F/m
V	1	8.717 kV	8.717 kV

where g_0 is the reference gravitational acceleration. In this study, g_0 = 0.00003. Electric Bond number Bo_e, which could be expressed as Eq. (37), is introduced to describe the ratio between electric field force and surface tension.

$$Bo_e = \frac{\varepsilon_0\varepsilon_L E_0^2 l_0}{\gamma} \tag{37}$$

where E_0 is the characteristic electric field intensity, which takes the value of the local electric field intensity at point "A" in Fig. 3(b).

Using the LBM, numerical simulations are usually conducted in lattice units. In this study, all of the values of the quantities are based on the lattice unit with the lattice constant $c = dx/dt = 1$ and $dx = dt = 1$, and the unit conversion from lattice unit to physical unit is also given in Table 2.

It is undeniable that the density ratio between liquid and gas at present study is much smaller than that in practical engineering applications. To overcome this issue, the numerical scheme in Refs. [31,36,37] could be adopted. Concretely, according to the numerical results in Refs. [31,36,37], a smaller a in Eq. (14) could result in a thicker interface and a smaller spurious current. Since the rapid change

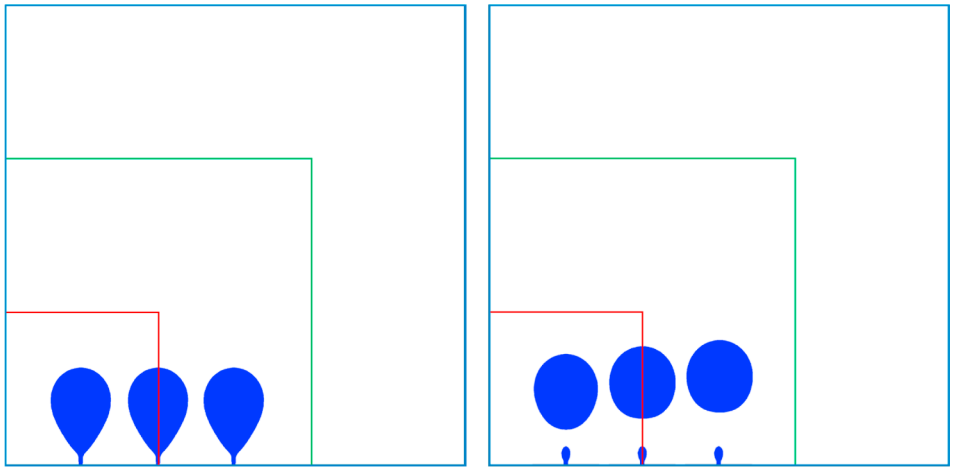

(a) $t^* = 6.56$ (b) $t^* = 8.20$

Fig. 4. The effect of domain size on bubble growing, detachment and rising processes.

of physical properties at the interface can be smoothed by a thicker interface, a smaller a will allow us to simulate multiphase flow at a larger density ratio. For example, in the numerical study of Fang et al. [37], the parameter a was set to be 0.02267 and the saturated temperature is set to be $0.68T_c$. The density ratio between liquid and gas in their study could be as higher as 200.

4.2. Convergence study

To obtain reasonable numerical results, a convergence study is required. In this section, the gravitational acceleration and electric field intensity are $g = g_0$ and $E_0 = 0$, respectively. Three different domain sizes (including 100 × 100, 200 × 200 and 300 × 300) are performed. Fig. 4 represents the effect of domain size on bubble growing, detachment and rising processes. As shown in Fig. 4, the domain size has little effect on the bubble growing and detachment processes. However, it has an obvious effect on the bubble rise. In further study, when the 100 × 100 domain size is adopted in the simulations under microgravity, it is found that the vapor bubble will almost fill up the whole computation domain before its departure. Thus the 100 × 100 domain size is not adopted in our simulations. As shown in Fig. 4, the numerical results of all of these three meshes in the bubble growing and detachment processes are the same. In other words, the domain size has no effect on departure diameter, shape and time. Therefore, the 200 × 200 domain size is adopted in the following simulations for the sake of time and memory optimization, although the 300 × 300 domain size is better.

4.3. Bubble dynamics during pool nucleate boiling in absence of an electric field

Fig. 5 represents the evolution of bubble contours during pool nucleate boiling under normal gravity (i.e., $g = g_0$) when electric field is absent (i.e., $Bo_e = 0$), where $t^* = t/t_0$. As shown in Fig. 5, at $t^* = 2.34$, a vapor bubble has been nucleated on the center of the bottom wall owing to the high temperature. From $t^* = 2.34$ to $t^* = 6.08$, with the growth of vapor bubble, bubble size increases rapidly. In addition, the height of vapor bubble increases obviously. It's because the vapor bubble tends to depart away from the horizontal wall under the effect of buoyancy. At $t^* = 4.21$, due to the action of buoyancy, a "neck" is formed during the process of bubble growth. From $t^* = 4.21$ to $t^* = 6.08$, the width of the "neck" decreases gradually, indicating that the tendency of bubble detachment becomes stronger. At $t^* = 7.95$, the bubble breaks at the "neck" and departs away from the horizontal wall. In the meantime, a small amount of vapor still remains at the horizontal wall and will grow to be a new vapor bubble after a while.

Fig. 6 displays the evolution of bubble contours during pool nucleate boiling under microgravity conditions (i.e., $g = g_0/4$ and $g = g_0/6$) when electric field is absent (i.e., $Bo_e = 0$). Compared with Fig. 5, due to the rapid decrease in buoyancy, bubble release period (i.e., the inverse of bubble release frequency) and bubble departure diameter increase obviously. In addition, decreasing gravitational acceleration would increase the width of vapor bubble. Assuming that there are other bubbles nucleated around, it's more likely for the vapor bubble to coalesce with other bubbles to form a large bubble or even steam film under microgravity conditions. Therefore, heat transfer deterioration might take place due to the delay in bubble detachment.

Fig. 7(a) represents the influence of gravitational acceleration on bubble departure diameter. D_d^* is the dimensionless bubble departure diameter, $D_d^* = D_d/l_0$ and D_d is the bubble departure diameter. As shown in Fig. 7(a), bubble departure diameter increases gradually with a decrease in gravitational acceleration. The relationship between bubble departure diameter and gravitational acceleration is $D_d^* = 1.976(g/g_0)^{-0.509}$. This result agrees well with the theoretical correlation of Fritz [38], proving the rationality of the numerical results in this paper. Fig. 7(b) displays the influence of gravitational acceleration on bubble release frequency, where f is the dimensionless bubble release frequency, $f = t_0/t_g$, and t_g is the bubble growth period. As shown in Fig. 7(b), decreasing gravitational acceleration would decrease the bubble release frequency, indicating that the bubble detachment becomes harder under microgravity. The relationship between bubble release frequency and gravitational acceleration is $f^{-1} = 6.381(g/g_0)^{-0.73}$. This result is in consistent with the numerical results of Gong and Cheng [39], confirming the rationality of the numerical results in this paper once again. In addition, it can be inferred from Fig. 7 that bubble detachment will be more difficult, bubble departure diameter will increase and bubble release frequency will decrease if gravitational acceleration decreases further. In this case, nucleate boiling might be converted into film boiling due to the delay of bubble detachment. Heat transfer deterioration and even the burnout of heated surface might take place.

4.4. Bubble dynamics during pool nucleate boiling in presence of an electric field

In this paper, a non-uniform electric field is provided by the charged metal sphere in Fig. 3(b). Fig. 8 displays the distributions of electric potentials, electric field intensities and electric streamlines within the computational domain. As shown in Fig. 8, the value of electric potential and electric field intensity reaches the maximum at the center of the bottom boundary, and the farther away from the center of the bottom boundary, the smaller the value of electric potential and electric field intensity is.

Fig. 9 displays the evolution of bubble contours during pool nucleate boiling under different electric field intensities. In Fig. 9, the gravitational acceleration $g = g_0/6$ and the electric potential at the surface of the charged metal sphere is set as $V_0 = 5$, 10, 15 and 20 (i.e., $Bo_e = 1.224$, 4.895, 11.014 and 19.580), respectively. Compare Fig. 9 with Fig. 6, it could be found that increasing electric field intensity could make the shape of the vapor bubble become slenderer and the deformation of vapor bubble become greater. In addition, increasing electric field intensity decreases bubble release period and bubble departure diameter obviously. This result proves that a non-uniform electric field could accelerate the detachment of vapor bubble. Moreover, increasing electric field intensity decreases the width of bubble obviously. As a result, the formation of large bubble or vapor film could

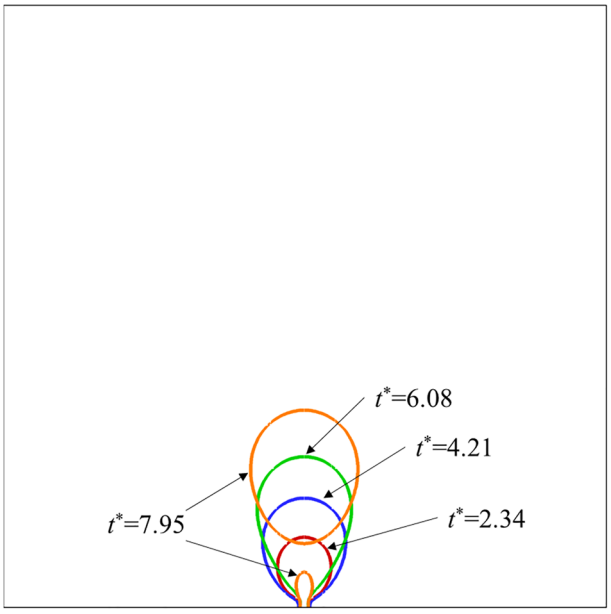

Fig. 5. Evolution of bubble contours during pool nucleate boiling at $g = g_0$ and $Bo_e = 0$.

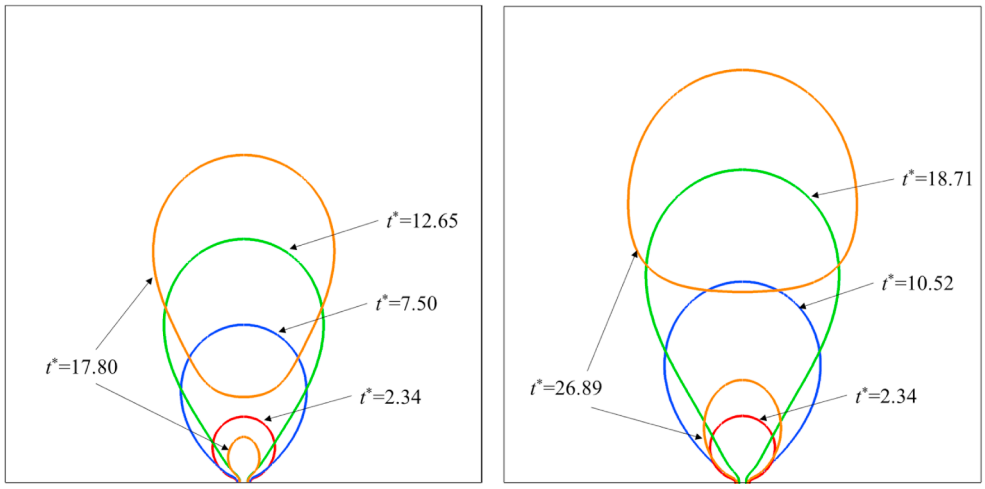

(a) $g=g_0/4$ (b) $g=g_0/6$

Fig. 6. Evolution of bubble contours during pool nucleate boiling under microgravity conditions (i.e., $g = g_0/4$ and $g = g_0/6$) when electric field is absent.

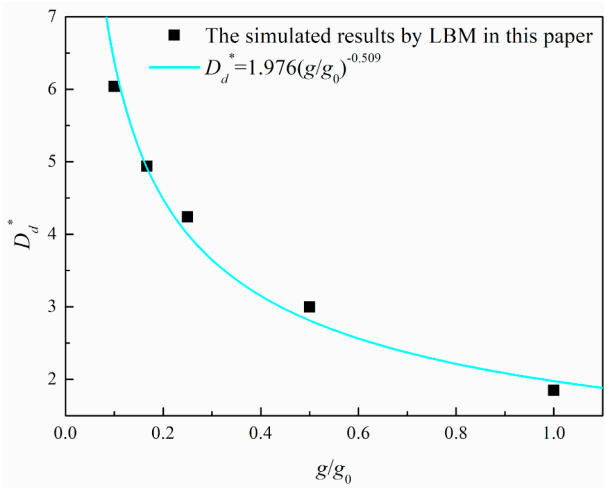

(a) Influence of gravitation acceleration on bubble departure diameter

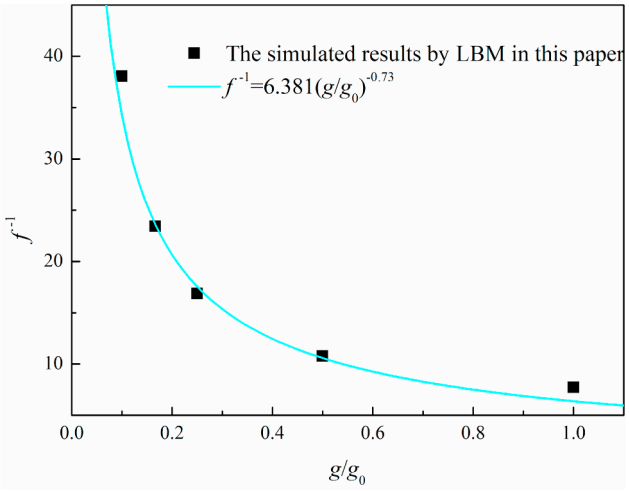

(b) Influence of gravitation acceleration on bubble release frequency

Fig. 7. Influence of gravitation acceleration on bubble departure diameter and bubble release frequency.

be prevented and heat transfer deterioration could be avoided to some extent under a non-uniform electric field.

Fig. 10(a) and (b) represent the distribution of velocity vectors around a vapor bubble during pool nucleate boiling at $t^* = 8.20$ without and with the effect of a non-uniform electric field, respectively. In Fig. 10, the gravitational acceleration is set as $g = 1/6g_0$, the blue curves represent the liquid-vapor phase interface and the arrows represent the velocity vectors. As shown in Fig. 10, a non-uniform electric field has an obvious influence on the velocity fields around a vapor bubble before it departs away from the horizontal wall. Firstly, the directions of the velocity vectors are modified by the non-uniform electric field. In Fig. 10(a), the velocity vectors are almost horizontal at the left side and right side of the vapor bubble. However, in Fig. 10(b), almost all of the velocity vectors inside the bubble are upward. This phenomenon indicates that the applied electric field could obviously modify the velocity fields around the vapor bubble before its detachment. As a result, the shape of the vapor bubble in Fig. 10(b) is much slenderer than that in Fig. 10(a). Secondly, the non-uniform electric field could obviously increase the magnitude of the averaged velocity inside of the vapor bubble (i.e., $\bar{u}_{y,B}$). In Fig. 10(a) and (b), $\bar{u}_{y,B}$ equals 0.0163 and 0.0207, respectively. As a result, the applied electric field would decrease the bubble departure diameter and increase the bubble release frequency.

Fig. 11 represents the effect of electric field intensity, which is characterized by Bo_e, on bubble equivalent diameter and bubble height at $g = g_0/6$. As shown in Fig. 11, at a given electric field intensity, the bubble height increases linearly over time, while the growth rate of bubble equivalent diameter decreases gradually. The difference between bubble height and bubble equivalent diameter increases over time. It's because buoyancy and electric force acted on bubble increase and the tendency of bubble detachment becomes stronger with the growth of vapor bubble. Therefore, the tensile deformation of bubble at the vertical direction is more pronounced. Besides, as shown in Fig. 11, bubble departure diameter and bubble release period decrease brightly with an increase in electric field intensity. However, electric field intensity has little effect on the growth rate of bubble equivalent diameter.

Fig. 12 displays the distribution of electric field forces acted on the phase interface before the bubble detachment. The directions of electric field forces are shown as arrows and the magnitude of electric field forces is described by color. As shown in Fig. 12, since the vapor bubble is symmetrical along y-axis, the total electric force acted on the whole phase interface at the horizontal direction equals 0. In other words, $\Sigma \mathbf{F}_e \cdot \mathbf{i} = 0$, where $\mathbf{F}_e$ is the electric field force acted on an arbitrary node

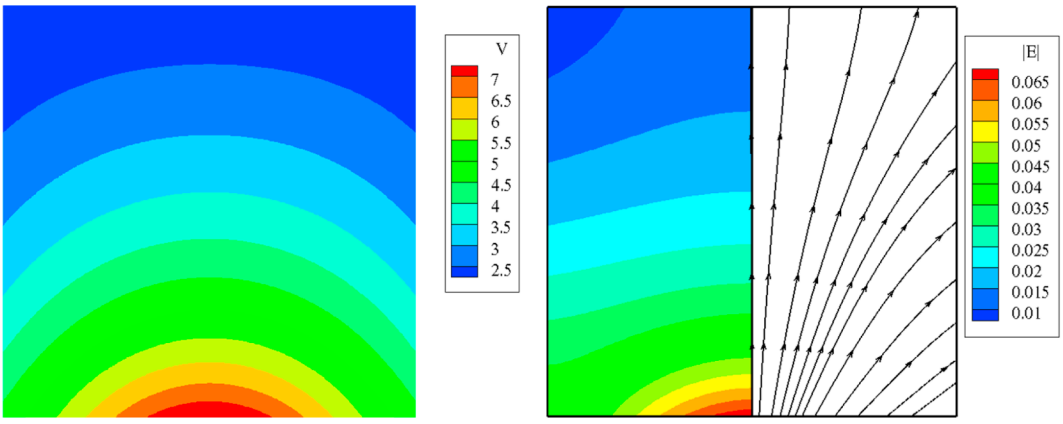

(a) V (b) **E** and electric streamlines

Fig. 8. Distribution of electric potentials V, electric field intensities **E** and electric streamlines within the computational domain (V_0 = 10).

of the phase interface, $\Sigma \mathbf{F}_e$ is the total electric field force acted on the whole phase interface, and **i** is the unit vector at the horizontal direction.

For convenience, as shown in Fig. 12, according to the angle between the phase interface and the horizontal wall, the phase interface can be divided into three regions. The Region A is the "neck" which is formed due to the tendency of the bubble detachment. At Region A, the phase interface is almost vertical to the horizontal wall. At Region B,

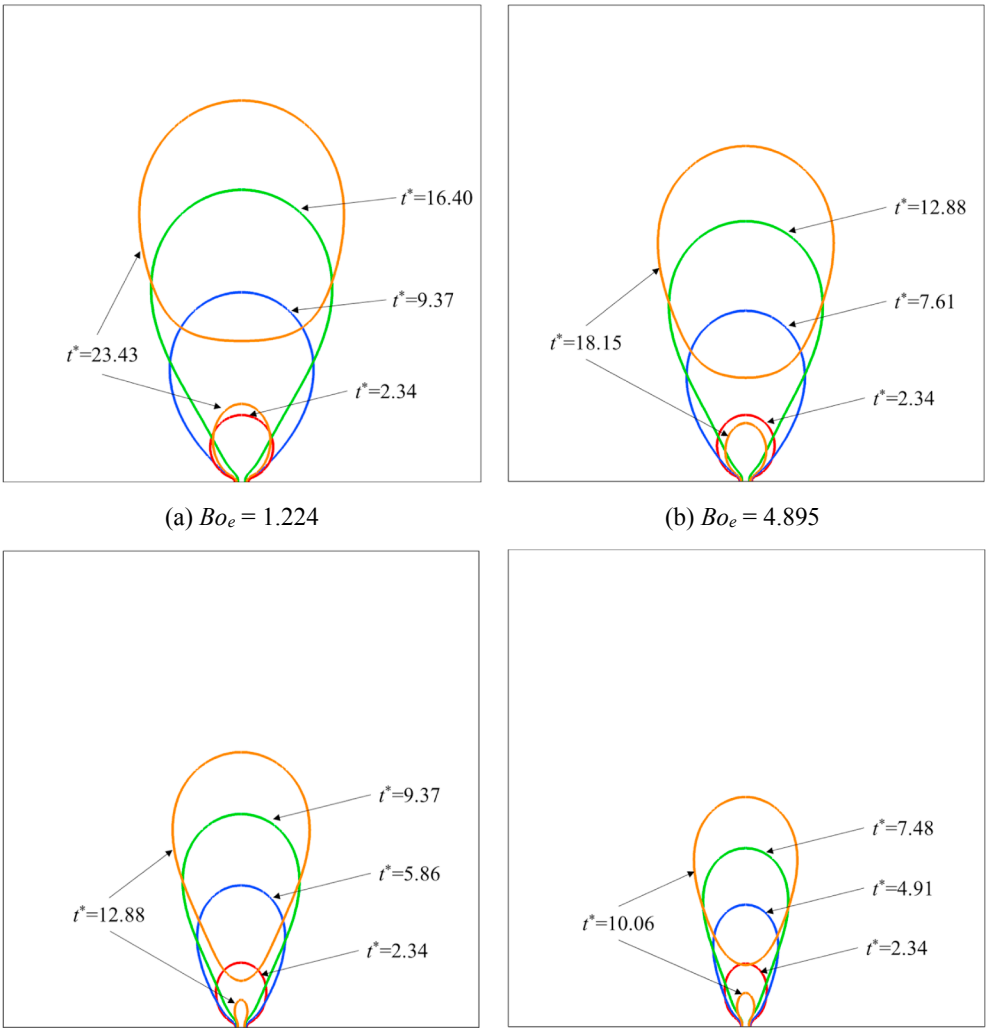

(a) Bo_e = 1.224 (b) Bo_e = 4.895

(c) Bo_e = 11.014 (d) Bo_e = 19.580

Fig. 9. Evolution of bubble contours during pool nucleate boiling under different electric field intensities ($g = g_0/6$).

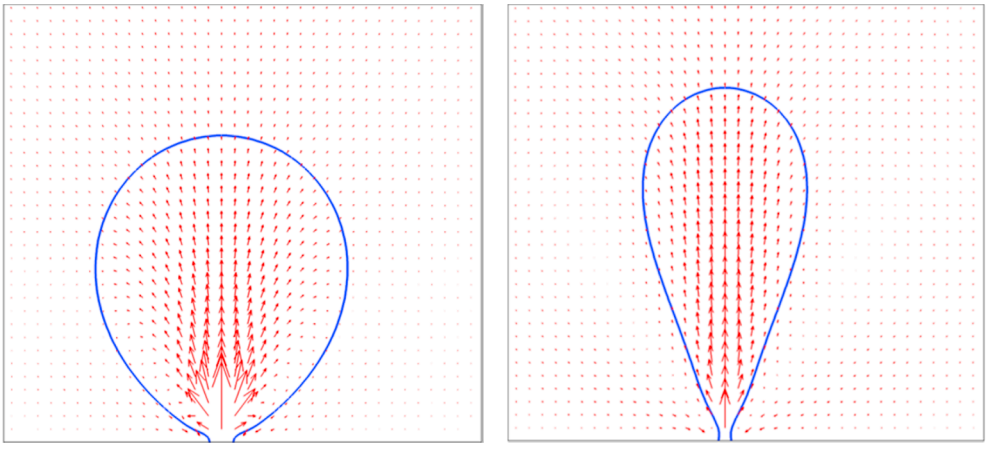

(a) Bo_e=0 (b) Bo_e=19.580

Fig. 10. The distribution of velocity vectors around a vapor bubble during pool nucleate boiling under the condition of $g = 1/6g_0$ at $t^* = 8.20$.

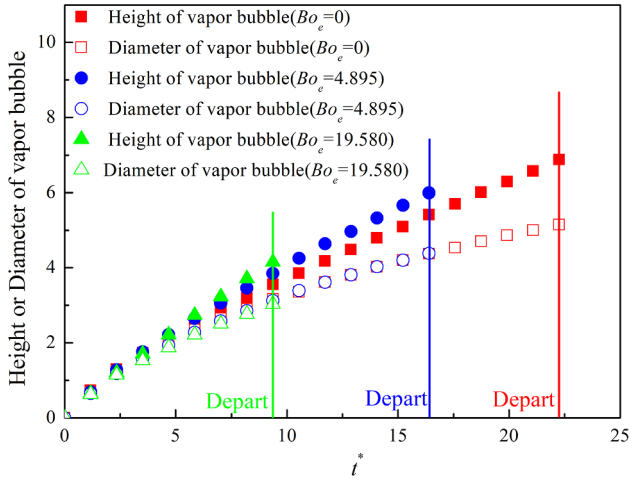

Fig. 11. Effect of electric field intensity on the evolution of bubble equivalent diameter and bubble height at $g = g_0/6$.

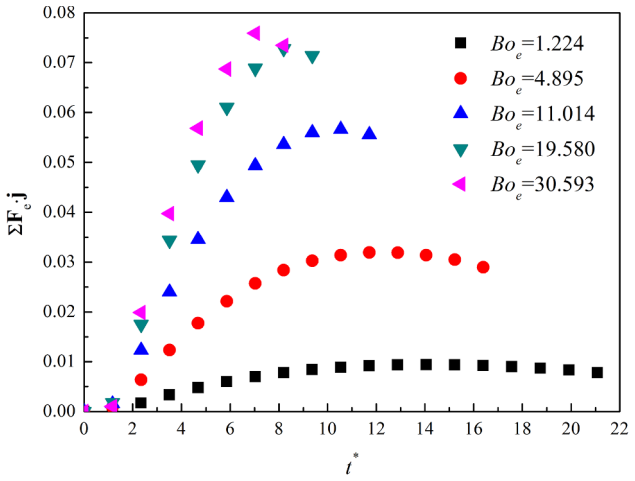

Fig. 13. Evolution of the total electric field force in the *y*-axis before the bubble detachment under different electric field intensities ($g = 1/6g_0$).

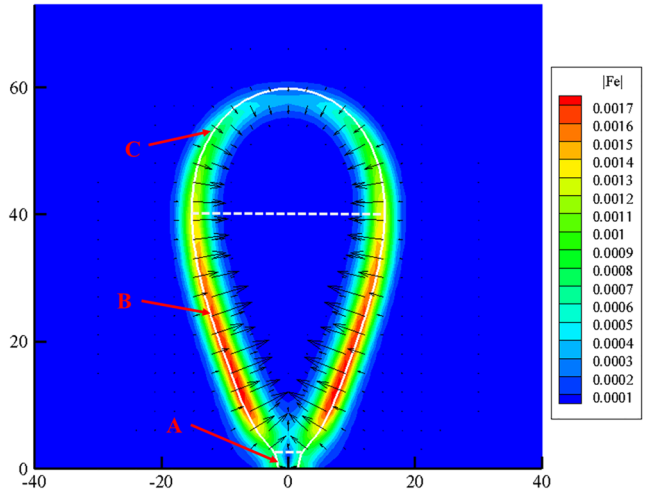

Fig. 12. Distribution of electric field forces around a vapor bubble before it departs away from the horizontal wall ($g = 1/6g_0$, $Bo_e = 19.580$, $t^* = 5.85$).

the angle between the phase interface and the horizontal wall is an obtuse angle. At Region C, the angle between the phase interface and the horizontal wall is an acute angle. The total electric force acted on the whole phase interface at the vertical direction can be expressed as Eq. (38).

$$\sum \mathbf{F}_e\cdot\mathbf{j} = \int_{A_T} \mathbf{F}_e\cdot\mathbf{j}\,dA = \int_{A_A} \mathbf{F}_e\cdot\mathbf{j}\,dA + \int_{A_B} \mathbf{F}_e\cdot\mathbf{j}\,dA + \int_{A_C} \mathbf{F}_e\cdot\mathbf{j}\,dA \tag{38}$$

where $\mathbf{j}$ is the unit vector at the vertical direction, A_T is the total area of the phase interface. A_A, A_B and A_C are the area of Region A, B and C, respectively. Obviously, $A_T = A_A + A_B + A_C$. As shown in Fig. 12, the electric field forces are perpendicular to the phase interface and point to the bubble interior, thus $\int_{A_A} \mathbf{F}_e\cdot\mathbf{j}\,dA = 0$, $\int_{A_B} \mathbf{F}_e\cdot\mathbf{j}\,dA > 0$ and $\int_{A_C} \mathbf{F}_e\cdot\mathbf{j}\,dA < 0$. According to Fig. 8 and Eq. (20), moving away from the center of the bottom boundary results in a decrease in electric field intensity and electric field force. Therefore, $\left|\int_{A_B} \mathbf{F}_e\cdot\mathbf{j}\,dA\right| > \left|\int_{A_C} \mathbf{F}_e\cdot\mathbf{j}\,dA\right|$ and $\Sigma\mathbf{F}_e\cdot\mathbf{j} > 0$. It can be concluded that the non-uniform electric field in Fig. 8 has the similar effect as buoyancy and could accelerate the detachment of bubble.

Fig. 13 represents the evolution of $\Sigma\mathbf{F}_e \cdot \mathbf{j}$ before the detachment of bubble under different Bo_e. As shown in Fig. 13, the value of $\Sigma\mathbf{F}_e \cdot \mathbf{j}$ firstly increases and then decreases over time. When the bubble size is small, the bubble height and bubble equivalent diameter increases gradually over time. According to Fig. 8, the electric field intensity at

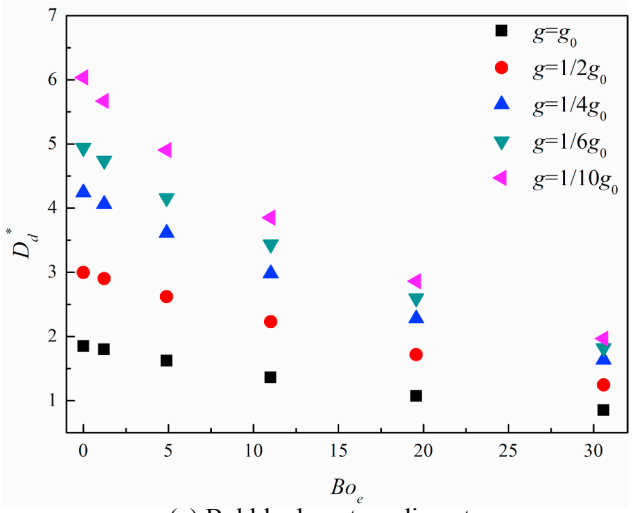

(a) Bubble departure diameter

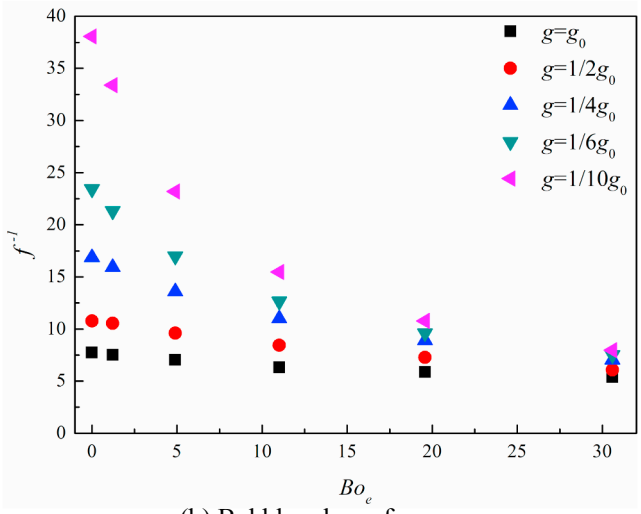

(b) Bubble release frequency

Fig. 14. Effect of electric field intensity on bubble departure diameter and bubble release frequency under different gravitational accelerations.

the top region of the bubble decreases, while the electric field intensity at the bottom region of the bubble keeps almost unchanged. Therefore, $\Sigma\mathbf{F}_e \cdot \mathbf{j}$ increases. With the further growth of the bubble, under the action of electric field force and buoyancy, a "neck" (i.e., the Region A in Fig. 12) will appear at the bottom region of the bubble. With an increase in the height of the "neck", the Region B and Region C in Fig. 12 are gradually moving away from the wall. Therefore, both $\left|\int_{A_B} \mathbf{F}_e \cdot \mathbf{j} dA\right|$ and $\left|\int_{A_C} \mathbf{F}_e \cdot \mathbf{j} dA\right|$ decrease. However, as shown in Fig. 8, the closer to the center of the bottom boundary, the greater the gradient of the electric field intensity is. Thus, the decrease rate of $\left|\int_{A_B} \mathbf{F}_e \cdot \mathbf{j} dA\right|$ is larger than that of $\left|\int_{A_C} \mathbf{F}_e \cdot \mathbf{j} dA\right|$. As a result, the value of $\Sigma\mathbf{F}_e \cdot \mathbf{j}$ starts to decrease after it reaches a maximum, as shown in Fig. 13. In addition, increasing electric field intensity could increase the value of $\Sigma\mathbf{F}_e \cdot \mathbf{j}$ and make evolution of $\Sigma\mathbf{F}_e \cdot \mathbf{j}$ becomes more intense.

Fig. 14 represents the effect of Bo_e on bubble departure diameter and bubble release frequency under different gravitational accelerations. As shown in Fig. 14, when electric field intensity remains unchanged, with a decrease in gravitational acceleration, bubble departure diameter increases, while bubble release frequency decreases. When gravitational acceleration remains unchanged, with an increase in electric field intensity, bubble departure diameter decreases, while bubble release frequency increases. In addition, as shown in Fig. 14, decreasing gravitational acceleration could strengthen the influence of electric field intensity on bubble departure diameter and bubble release frequency, indicating that the electric field in Fig. 8 could effectively accelerate the detachment of bubble and reduce the possibility of heat transfer deterioration under microgravity.

5. Concluding remarks

In this paper, the two-dimensional lattice Boltzmann model was developed to simulate the pool boiling in presence of an external electric field. In this model, the pseudopotential model was coupled with phase-change model and electric field model. The growth and detachment of a single bubble on the horizontal wall during pool nucleate boiling under the effect of a non-uniform electric field was simulated. The influence of gravitational acceleration and electric field intensity on bubble departure diameter and bubble release frequency was investigated, and the influencing mechanism of the non-uniform electric field on bubble dynamics during nucleate boiling was analyzed. Based on the numerical results, it could be concluded that:

1. With a decrease in gravitational acceleration, the detachment of bubble became harder, bubble departure diameter increased, and bubble release frequency decreased. Therefore, due to the delay of bubble detachment under microgravity, a vapor film might be formed, the nucleate boiling might be converted into film boiling, and heat transfer deterioration might take place.
2. Under the same gravitational acceleration, with an increase in electric field intensity, bubble departure diameter decreased, bubble release frequency increased, indicating that the electric field force could accelerate the detachment of vapor bubble.
3. Decreasing gravitational acceleration could enhance the influence of electric field intensity on bubble departure diameter and bubble release frequency. Therefore, the non-uniform electric field established in this study contributed very much to the departure of bubbles under microgravity conditions. As a result, the occurrence rate of film boiling declines and the heat transfer capacity could be improved under the non-uniform electric field.
4. The total electric field force in the vertical direction increased firstly and then decreased over time before the departure of the vapor bubble from the horizontal wall. In addition, increasing electric field intensity could make the evolution of total electric field force became more intense.

Acknowledgement

This work is supported financially by the joint fund between the Chinese Academy of Sciences (CAS) and National Natural Science Foundation of China (NSFC) under the Grant of U1738105.

Appendix A. Determination of the surface tension and contact angle

According to the Laplace equation of capillary, the pressure difference across the interface of a droplet with a radius of R_b in equilibrium is

$$\Delta P = \gamma / R_b \tag{A.1}$$

where ΔP is the pressure difference between inside and outside of the droplet. In order to obtain the surface tension γ, saturated droplets of different radii suspended in the saturated vapor in a 200 × 200 domain, with zero gravity at $T_{sat} = 0.86T_c$, are simulated by the two-phase flow model in

Section 2.1. The simulation results of ΔP versus $1/R_b$ are given in Fig A.1. As shown, the simulated results can be fitted with a straight line having a slope of 0.0878. According to equation (A.1), the surface tension between the saturated liquid and vapor at $T_{sat} = 0.86T_c$ is 0.0878.

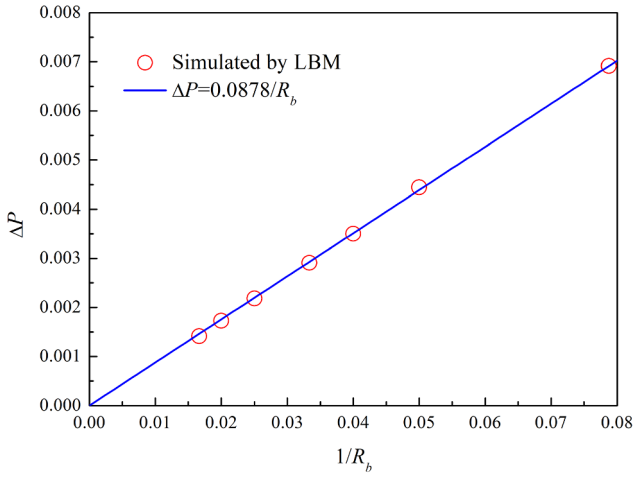

Fig. A.1. Influence of droplet radius on the pressure difference of the droplet.

Wettability of the heating surface, characterized by the contact angle, is an important parameter influencing pool boiling heat transfer. The static contact angle can be tuned by the fluid-solid interaction strength G_w in Eq. (11). In this study, $G_w = 0$ is adopted and the intermolecular interaction force in Eq. (11) is not applied at the solid walls. To determine the static contact angle under this condition, a saturated droplet with a radius of $R_b = 40$ is placed on the non-slip bottom wall in a 300×100 lattice domain under zero gravity. The saturated droplet is surrounded by the saturated vapor at $T_{sat} = 0.86T_c$. Periodic boundary condition is imposed in x direction and the no-slip boundary condition. Using the two-phase flow model in Section 2.1, the final equilibrium shape of the droplet is presented in Fig A.2., where the static contact angle is measured to be 44.5°.

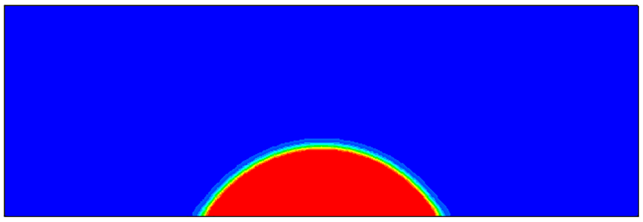

Fig. A.2. The balance form of droplet on a horizontal surface.

References

[1] M. Gao, P. Cheng, X. Quan, An experimental investigation on effects of an electric field on bubble growth on a small heater in pool boiling, Int. J. Heat Mass Transf. 67 (2013) 984–991.

[2] X. Quan, M. Gao, P. Cheng, J. Li, An experimental investigation of pool boiling heat transfer on smooth/rib surfaces under an electric field, Int. J. Heat Mass Transf. 85 (2015) 595–608.

[3] Y.H. Diao, L. Guo, Y. Liu, Y.H. Zhao, S. Wang, Electric field effect on the bubble behavior and enhanced heat-transfer characteristic of a surface with rectangular microgrooves, Int. J. Heat Mass Transf. 78 (2014) 371–379.

[4] N. Schweizer, P.D. Marco, P. Stephan, Investigation of wall temperature and heat flux distribution during nucleate boiling in the presence of an electric field and in variable gravity, Exp. Therm Fluid Sci. 44 (2013) 419–430.

[5] C.C. Pascual, S.M. Jeter, S.I. Abdel-Khalik, A statistical analysis of EHD-enhanced nucleate boiling along a heated wire, Int. J. Heat Mass Transf. 44 (2001) 1201–1212.

[6] S. Siedel, S. Cioulachtjian, A.J. Robinson, J. Bonjour, Electric field effects during nucleate boiling from an artificial nucleation site, Exp. Therm Fluid Sci. 35 (2011) 762–771.

[7] M.S. Shadloo, A. Rahmat, M.J.C.M. Yildiz, A smoothed particle hydrodynamics study on the electrohydrodynamic deformation of a droplet suspended in a neutrally buoyant Newtonian fluid, Comput. Mech. 52 (2013) 693–707.

[8] Q. Yang, B.Q. Li, J. Shao, Y. Ding, A phase field numerical study of 3D bubble rising in viscous fluids under an electric field, Int. J. Heat Mass Transf. 78 (2014) 820–829.

[9] T. Wang, H.X. Li, Y.F. Zhang, D.X. Shi, Numerical simulation of bubble dynamics in a uniform electric field by the adaptive 3D-VOSET method, Numerical Heat Transfer, Part A: Applications 67 (2015) 1352–1369.

[10] S.W.J. Welch, G. Biswas, Direct simulation of film boiling including electrohydrodynamic forces, Phys. Fluids 19 (2007) 012106.

[11] G. Tomar, G. Biswas, A. Sharma, S.W.J. Welch, Influence of electric field on saturated film boiling, Phys. Fluids 21 (2009) 032107.

[12] V. Pandey, G. Biswas, A. Dalal, Saturated film boiling at various gravity levels under the influence of electrohydrodynamic forces, Phys. Fluids 29 (2017) 032104.

[13] Y. Hristov, D. Zhao, D.B.R. Kenning, K. Sefiane, T.G. Karayiannis, A study of nucleate boiling and critical heat flux with EHD enhancement, Heat Mass Transf. 45 (2009) 999–1017.

[14] Z.L. Guo, C.G. Zheng, Theory and applications of lattice Boltzmann method, Science, Beijing, 2009.

[15] S. Chen, G.D. Doolen, Lattice Boltzmann method for fluid flows, Ann. Rev. Fluid Mech. 30 (1998) 329–364.

[16] A.A. Mohamad, Lattice Boltzmann Method: Fundamentals and Engineering Applications with Computer Codes, Springer Science & Business Media, 2011.

[17] A. Xu, W. Shyy, T. Zhao, Lattice Boltzmann modeling of transport phenomena in fuel cells and flow batteries, Acta Mechanica Sinica 33 (2017) 555–574.

[18] H. Huang, M.C. Sukop, X.Y. Lu, Multiphase Lattice Boltzmann Methods: Theory and Application, Wiley-Blackwell, Chichester, West Sussex, 2015.

[19] Z. Dong, W. Li, Y. Song, A numerical investigation of bubble growth on and departure from a superheated wall by lattice Boltzmann method, Int. J. Heat Mass Transf. 53 (2010) 4908–4916.

[20] T. Sun, W. Li, Three-dimensional numerical simulation of nucleate boiling bubble by lattice Boltzmann method, Comput. Fluids 88 (2013) 400–409.

[21] R. Sadeghi, M.S. Shadloo, M.Y.A. Jamalabadi, A. Karimipour, A three-dimensional lattice Boltzmann model for numerical investigation of bubble growth in pool boiling, Int. Commun. Heat Mass Transf. 79 (2016) 58–66.

[22] R. Sadeghi, M.S. Shadloo, Three-dimensional numerical investigation of film boiling by the lattice Boltzmann method, Numer. Heat Transf., Part A: Appl. 71 (2017) 560–574.

[23] Y. Feng, H. Li, K. Guo, J. Zhao, T. Wang, Numerical study of single bubble growth on and departure from a horizontal superheated wall by three-dimensional lattice Boltzmann method, Microgravity Sci. Technol. 30 (2018) 761–773.

[24] T. Sun, W. Li, S. Yang, Numerical simulation of bubble growth and departure during flow boiling period by lattice Boltzmann method, Int. J. Heat Fluid Flow 44 (2013) 120–129.
[25] X. Shan, H. Chen, Lattice Boltzmann model for simulating flows with multiple phases and components, Phys. Rev. E: Stat. Phys. Plasmas Fluids Relat. Interdiscip. Top. 47 (1993) 1815–1819.
[26] G. Hazi, A. Markus, On the bubble departure diameter and release frequency based on numerical simulation results, Int. J. Heat Mass Transf. 52 (2009) 1472–1480.
[27] S. Gong, P. Cheng, Numerical simulation of pool boiling heat transfer on smooth surfaces with mixed wettability by lattice Boltzmann method, Int. J. Heat Mass Transf. 80 (2015) 206–216.
[28] S. Gong, P. Cheng, Direct numerical simulations of pool boiling curves including heater's thermal responses and the effect of vapor phase's thermal conductivity, Int. Commun. Heat Mass Transf. 87 (2017) 61–71.
[29] X. Ma, P. Cheng, S. Gong, X. Quan, Mesoscale simulations of saturated pool boiling heat transfer under microgravity conditions, Int. J. Heat Mass Transf. 114 (2017) 453–457.
[30] Q. Li, Q.J. Kang, M.M. Francois, Y.L. He, K.H. Luo, Lattice Boltzmann modeling of boiling heat transfer: the boiling curve and the effects of wettability, Int. J. Heat Mass Transf. 85 (2015) 787–796.
[31] Q. Li, K.H. Luo, X.J. Li, Lattice Boltzmann modeling of multiphase flows at large density ratio with an improved pseudopotential model, Phys. Rev. E Stat. Nonlin. Soft. Matter. Phys. 87 (2013) 053301.
[32] W. Tai, VOSET Method based on adaptive cartesian grid with application in investigation on bubble dynamics in electric fields, in: Vol. Doctor, Xi'an Jiaotong University, 2016.
[33] S. Gong, P. Cheng, X. Quan, Lattice Boltzmann simulation of droplet formation in microchannels under an electric field, Int. J. Heat Mass Transf. 53 (2010) 5863–5870.
[34] C.K. Law, Recent advances in droplet vaporization and combustion, Prog. Energy Combust. Sci. 8 (1982) 171–201.
[35] Q. Li, P. Zhou, H.J. Yan, Improved thermal lattice Boltzmann model for simulation of liquid-vapor phase change, Phys. Rev. E 96 (2017) 063303.
[36] A. Xu, T.S. Zhao, L. An, L. Shi, A three-dimensional pseudo-potential-based lattice Boltzmann model for multiphase flows with large density ratio and variable surface tension, Int. J. Heat Fluid Flow 56 (2015) 261–271.
[37] W.Z. Fang, L. Chen, Q.J. Kang, W.Q. Tao, Lattice Boltzmann modeling of pool boiling with large liquid-gas density ratio, Int. J. Therm. Sci. 114 (2017) 172–183.
[38] W. Fritz, Maximum volume of vapor bubbles, Phys. Z. 36 (1935) 379–388.
[39] S. Gong, P. Cheng, Lattice Boltzmann simulation of periodic bubble nucleation, growth and departure from a heated surface in pool boiling, Int. J. Heat Mass Transf. 64 (2013) 122–132.